

Monte Carlo simulation of grain growth and welding zones in friction stir welding of AA6082-T6

Z. Zhang¹ · Q. Wu¹ · M. Grujicic² · Z. Y. Wan¹

Received: 23 April 2015 / Accepted: 10 October 2015 / Published online: 2 November 2015
© Springer Science+Business Media New York 2015

Abstract Adaptive remeshing finite element model is used for the prediction of material behavior and temperature histories in friction stir welding (FSW). Then, Monte Carlo method with nucleation in every MC step is used for the simulation of the grain growth in FSW. In addition, the process of dynamic recrystallization which results in the nucleation of new grains has been modeled. The model is validated by comparison of both experiments and numerical results from the literature. The width of the stirring zone has been estimated by monitoring the movements of the traced material particles and by identifying the region containing dynamically recrystallized fine grains. The inner border of the heat-affected zone has been determined by monitoring the material flow, while the outer border has been identified by monitoring the average grain size as a function of the lateral distance from the weld. The effect of two FSW process parameters, tool rotational speed and tool shoulder diameter, is investigated. An increase in either of these two parameters has been found to increase the overall grain size as well as the width of the welding zones.

Introduction

As an important solid-state joining technique, friction stir welding (FSW) has been widely used in industries [1, 2]. In FSW, the welding tool is inserted into the welding line. A tight joint can be then formed with the rotation and transverse movement of the welding tool. Both the heat generations and the material flows can affect the microstructural evolutions in the welding zone [3, 4]. According to the different microstructures, the welding zone can be divided into different regions: the stirring zone (SZ), the thermo-mechanically affected zone (TMAZ), and the heat-affected zone (HAZ) [5, 6]. The changes of the microstructures in the welding zone can obviously affect the mechanical properties of friction stir-welded joints, i.e., the hardness [7–9], the tensile strength [10], the fatigue properties [11, 12], the corrosion resistance [13, 14], etc. This is the reason for the development of the numerous numerical models on the microstructural evolutions. Polycrystal plasticity and CFD model were used by Cho et al. [15] for the prediction of the texture evolutions in the welding zone. A smoothed particle hydrodynamics model was established by Pan et al. [16] for the simulation of grain sizes, textures, and microhardness in FSW of AZ31. The cellular automata finite element (CAFE) model was used by Saluja et al. [17] to predict the grain size distribution during FSW and the influence of weld defects on the forming of FSW sheets. Arora et al. [18] simulated the temperature distribution and estimated the grain size during FSW by using finite difference equations. A chain of integrated models were developed by Simar et al. [19] to study various properties related to microstructure evolution during FSW. The hardness profile and the evolution of relevant strengthening precipitates across the welds were studied by Hersent et al. [20] in FSW of 2024-T3 aluminum alloy. Buffa et al. [21] investigated the micro- and macro-

✉ Z. Zhang
zhangz@dlut.edu.cn

¹ State Key Laboratory of Structural Analysis for Industrial Equipment, Department of Engineering Mechanics, Faculty of Vehicle Engineering and Mechanics, Dalian University of Technology, Dalian 116024, China

² Department of Mechanical Engineering, Clemson University, 241 Engineering Innovation Building, Clemson, SC 29634-0921, USA

mechanical characteristics of friction stir-welded Ti-6Al-4V lap joints numerically and experimentally.

Monte Carlo (MC) method is valid and efficient for the prediction of grain growth and topological features. The application aspects of MC method include the fields of welding [22, 23], abnormal and anisotropic grain growth [24, 25], grapheme growth [26], polycrystalline microstructures [27], etc. Details of the MC technique can be found in the literature [25, 28, 29].

Grain evolution in welding zones is one of the key factors for the determination of the sizes of the HAZ and SZ, which is very important for the controlling of the welding quality and for the investigation on the FSW mechanism. Detailed grain growth process in FSW has seldom been reported. So, MC method with consideration of nucleation rate in each MC step is implemented for the simulation of the grain growth in FSW of AA6082-T6 in the present work. The influences of the rotation speeds and the shoulder diameters on the microstructural changes are studied in detail. The regions of the welding zones are then determined from the predicted grains.

Model description

Finite element model

The dimensions of the welded plates are $80 \times 50 \times 3$ mm. The plates are initially meshed into 6265 nodes and 25152 elements in the commercial FEA code DEFORM-3D™, as shown in Fig. 1. In accordance with the simulation carried out in the previous work [30], the initial mesh size is taken as 0.75 mm in the regions in and near the welding zone, and the mesh sizes vary from 1.5 to 3 mm in the other regions. The physical and mechanical properties of the welding material AA6082-T6 are considered as the functions of temperatures [31]. Viscoplastic constitutive model

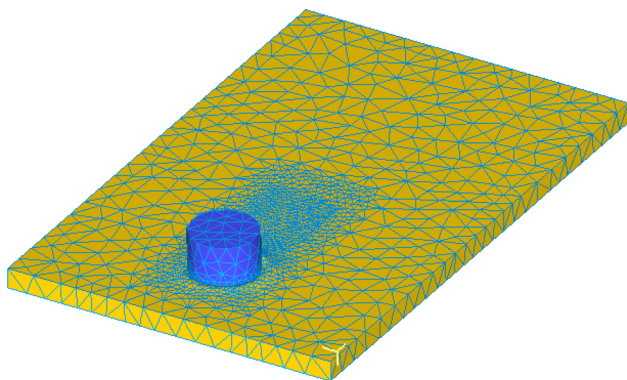


Fig. 1 FEM model of case 1

is used for the simulation of the material behaviors of the welding material [30],

$$\dot{\epsilon} = A_0 [\sinh(\alpha_0 \bar{\sigma})]^{n_0} e^{(-Q/RT_{\text{abs}})}, \tag{1}$$

where T_{abs} is the absolute temperature; Q is the activation energy; R is the Universal Gas Constant; n_0 , α_0 , and A_0 are equation coefficients, which are derived from the experimental tests [32]; and n_0 , α_0 , and A_0 are taken as 6.49, 0.0238, and 8.0×10^9 , respectively. $\dot{\epsilon}$ is the equivalent strain rate. $\bar{\sigma}$ is the flow stress.

The welding tool is simplified as a rigid body. Shear model is used for the definition of the contact behaviors on the tool-plate surface,

$$f = m_0 \cdot k, \tag{2}$$

where f is the frictional stress, k is the yield shear stress, and m_0 is the frictional factor and is taken as 0.3 to make sure that the model can match the measured tool forces and temperatures [33]. This value has been validated in the previous work [30, 34]. A limitation on the friction stress by shear failure can be valid especially for the cases in higher rotating speeds [35].

The influences of the different rotation speeds and shoulder diameters on the microstructures are then investigated in the welding zones. The welding parameters of the simulated cases are shown in Table 1. The adaptive remeshing finite element formulations are implemented in the computation process to solve the problems of mesh entanglements and distortions caused by the large deformation and the material flow in FSW. The details of the remeshing technique can be found in Ref. [30].

Air cooling condition is used after FSW to obtain the complete temperature histories which are used for the calculations on grain growth in the MC model. The boundaries of the welding plate are set to be at room temperature, and the convective heat transfer coefficient is set to be 30 W/(m²K).

Monte Carlo model

In the MC model, a two-dimensional matrix with lattice points $N \times N$ is used. The values on grid points represent the grain crystallographic orientations (1 ~ q). Adjacent grid points with the same grain crystallographic orientations are regarded as a grain. The free energy is determined by the present crystallographic orientation and neighborhood orientations at the randomly selected point. At each lattice point site, the grain-boundary energy is calculated by the Hamiltonian [22]:

$$E = -J \sum_{i=1}^m (\delta_{q_i, q_j} - 1), \tag{3}$$

Table 1 Welding parameters of the simulated cases

Case	Transverse speed v (mm/min)	Rotation speed w (r/min)	Shoulder diameter D (mm)	Pin diameter d (mm)
1	100	1000	10	3
2	100	1500	10	3
3	100	1000	13	3

where J is a positive constant which represents the grain-boundary energy, m is the total number of the sites near the lattice point, δ is the Kronecker symbol, and q_i is the orientation of the lattice point near the calculated grid site.

The grain growth is activated by the grain-boundary migration kinetics. For the randomly selected grain site, the change of the energy is determined by the change of the present crystallographic orientation to its neighborhood,

$$p = \begin{cases} 1, & \Delta E \leq 0 \\ e^{-\frac{\Delta E}{k_B T}} = e^{-\frac{(m_2 - m_1)J}{k_B T}}, & \Delta E > 0 \end{cases} \quad (4)$$

where ΔE is the change of grain-boundary energy due to reorientation, k_B is the Boltzmann constant, T is the temperature, and m_1 and m_2 are the number of different orientations before and after the reorientation. If $\Delta E \leq 0$, the new crystallographic orientation of the randomly selected grain site is accepted; else it is accepted with the Boltzmann probability [23, 36].

In one MC step, the algorithm described above is iterated for N^2 times. Through the MC simulation, the microstructure is represented by the orientation matrix. For the equiaxed grains, the average grain size is measured by the line intercept counting method. For microstructure with unequiaxed grains, the average grain size is computed from the average grain area:

$$L = \sqrt{\frac{S}{n_g}}, \quad (5)$$

where S is the simulated area and n_g is the number of grains in the simulated area. An empirically fitted relation between the simulated grain size and the number of MC steps can be obtained as [23]:

$$L = K_1 \lambda (MCS)^{n_1}, \quad (6)$$

where λ is the discrete grid spacing of the utilized grid model, and K_1 and n_1 are model constants which can be obtained from the simulated data by regression analysis.

In order to simulate the grain growth process in FSW, the relation between Monte Carlo steps and real time-temperature cycles of the welded material should be established. In the current work, the changing rate of the average grain size is assumed to be the function of the migration velocity of grain boundaries (v):

$$\frac{dL}{dt} = \alpha v^n, \quad (7)$$

where α and n are ratio constants, α is taken as 3.0 in HAZ and 1.0 in SZ, and n is taken as 0.1. The equation constants are used to make sure that the grain growth kinetics agree well with the real grain growth. The values used during the calculations are determined by trial and error method. v is defined as [28]:

$$v = \frac{AZV_m^2}{N_a^2 h} \exp\left(\frac{\Delta S_f}{R}\right) \exp\left(-\frac{Q}{RT}\right) \left(\frac{2\gamma}{L}\right), \quad (8)$$

where A , Z , V_m , R , N_a , and h are physical constants. ΔS_f and γ are material parameters of AA6082-T6. The material parameters and the ratio constants of AA6082-T6 used in Eqs. (7)–(8) are summarized in Table 2 [37–39]. From Eqs. (6)–(8), the relation between real time and MC steps can be obtained as the following discrete form:

$$(MCS)^{(n+1)n_1} = \left(\frac{L_0}{K_1 \lambda}\right)^{n+1} + \frac{(n+1)\alpha C_1^n}{(K_1 \lambda)^{n+1}} \sum \left[\exp^n\left(-\frac{Q}{RT_i}\right) t_i \right], \quad (9)$$

where $C_1 = \frac{2A\gamma ZV_m^2}{N_a^2 h} \exp\left(\frac{\Delta S_a}{R}\right)$, L_0 is initial average grain size, T_i is the average temperature in every time interval, and t_i represents the value of time interval.

In SZ, a 300×300 lattices system with randomly initial orientations is used to model the area in SZ of

Table 2 Material parameters and ratio constants [37–39]

Physical property	Value
Average number per unit area (Z)	4.31×10^{20} atoms/m ²
Planck's constant (h)	6.624×10^{-34} J s
Accommodation probability (A)	1.0
Avogadro's number (N_a)	6.02×10^{23} /mol
Atom molar volume (V_m)	1.0×10^{-5} m ³ /mol
Fusion entropy (ΔS_f)	11.5 J/mol/K
Activation enthalpy (Q)	140000 J/mol
Boundary energy (γ)	0.5 J/m ²
Gas constant (R)	8.31 J/mol/K
Ratio constant (α)	3.0 (HAZ and TMAZ), 1.0 (SZ)
Ratio constant (n)	0.1
DRX constant (N_0)	10^{24} (1/s/m ³)

500 × 500 μm². Materials in SZ undergo both high temperature and large plastic deformation. So, dynamic recrystallization (DRX) phenomenon should be considered in the simulation of grain growth. In this model, DRX procedure is simulated by implementing a nucleation rate in every MC step. The nucleation rate is considered as a function of both temperature and strain rate according to [40]:

$$\dot{n} = N_0 \dot{\epsilon} \exp\left(-\frac{Q}{RT}\right), \tag{10}$$

where N_0 is a constant and is taken as 10²⁴ (1/s/m³), $\dot{\epsilon}$ is the equivalent strain rate in SZ, which is assumed to be uniform in SZ and can be estimated by the following [41],

$$\dot{\epsilon} = \frac{w\pi r_e}{L_e}, \tag{11}$$

where r_e and L_e are the effective (or average) radius and depth of the dynamically recrystallized zone (SZ), respectively. r_e here is represented by 0.78 of the radius of SZ, and L_e is assumed to be the length of the pin. Number of nuclei in every MC step is calculated from the nucleation rate, and lattice points at grain boundary are picked to change to random orientations to create new nuclei. From Eq. (10), it can be seen that the nucleation rate is not a constant during the simulation. Higher temperature and equivalent strain rate can lead to higher nucleation rate.

Experimental results reported by Sato [42] are used to validate the simulation method of DRX in SZ. The simulated area is 500 × 500 μm², and the grid system was 300 × 300 in cases 1–3. The thermal cycles used are the same to the experimental measured values, and equivalent strain rates are calculated according to Eq. (11). Two working conditions with rotation speeds of 1600 rpm and 2450 rpm are modeled. The computed relationship between Log₁₀MCS and Log₁₀L is shown in Fig. 2, which

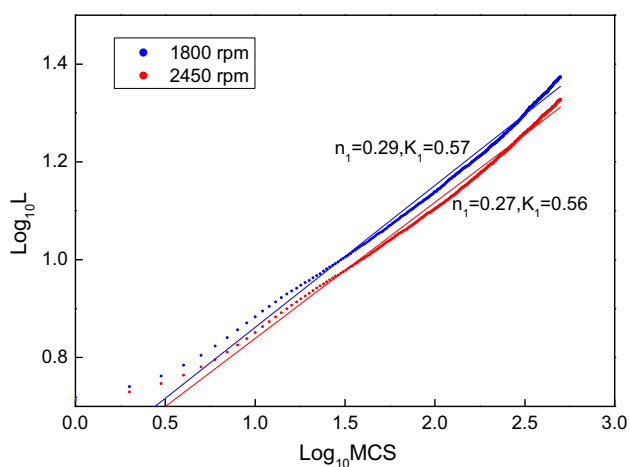


Fig. 2 Growth kinetics in SZ

Table 3 Validation of DRX simulation in SZ

	Measured (μm) [42]	Simulated (μm)	Error (%)
1600 rpm	12.28	13.27	8.1
2450 rpm	17.67	17.30	2.1

are used to determine the constants K_1 and n_1 . MC steps calculated from the two thermal cycles [42] are 119 and 216, respectively. Simulated average grain sizes agree well with the measured results, which can validate the simulation method used to model the DRX in SZ, as shown in Table 3. For further validation, friction stir-welded AA6082-T6 plate is modeled with the same welding conditions as the experimental conditions [43]. Average grain size in SZ is calculated by the MC method. The result is compared to the experimental observations [43] as summarized in Table 4. The error between the current numerical model and the experimental value is 6.2 %, suggesting that the present computational procedure can be used to predict grain-microstructure evolution during the FSW process with reasonable accuracy.

The initial grain size in HAZ is selected to be 80 μm according to experimental observation [43], and a 150 × 150 lattices system is used to model the area in HAZ of 1000 × 1000 μm². Randomly distributed Voronoi elements are used to model the initial distribution of the grains in HAZ. Material particles in TMAZ are affected by both mechanical elongation and temperature rises. For the determination of the stretch in TMAZ, two series of material particles on top and bottom surface of the plate at the cross section are traced. The initial distance between the two particles is 0.5 mm, as shown in Fig. 3. The flow behaviors of the traced material particles are used to distinguish the welding zones and to calculate the elongation of grains in TMAZ. A randomly generated configuration of grains with the same average elongation ratio calculated from traced particles is used to simulate the initial grain microstructure in TMAZ, and the lattice system used in TMAZ is the same of HAZ.

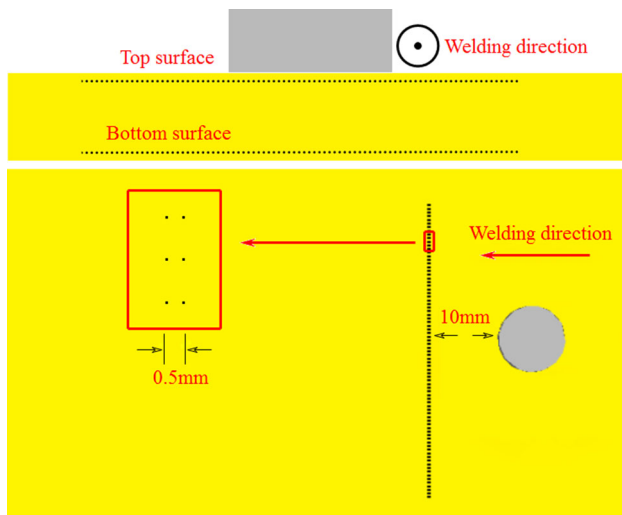
Results and discussion

Temperature distributions and materials flow

The calculated temperature fields of three cases are shown in Fig. 4. In the simulated cases, the temperature fields are symmetrical to the welding seam. The peak temperatures appear at the contacting surfaces of welding tools and the welding plates. In case 1, the peak temperature is 676 K. Both the increases in rotation speeds and shoulder diameters can lead to increased heat generation. When the

Table 4 Validation of predicted grain size

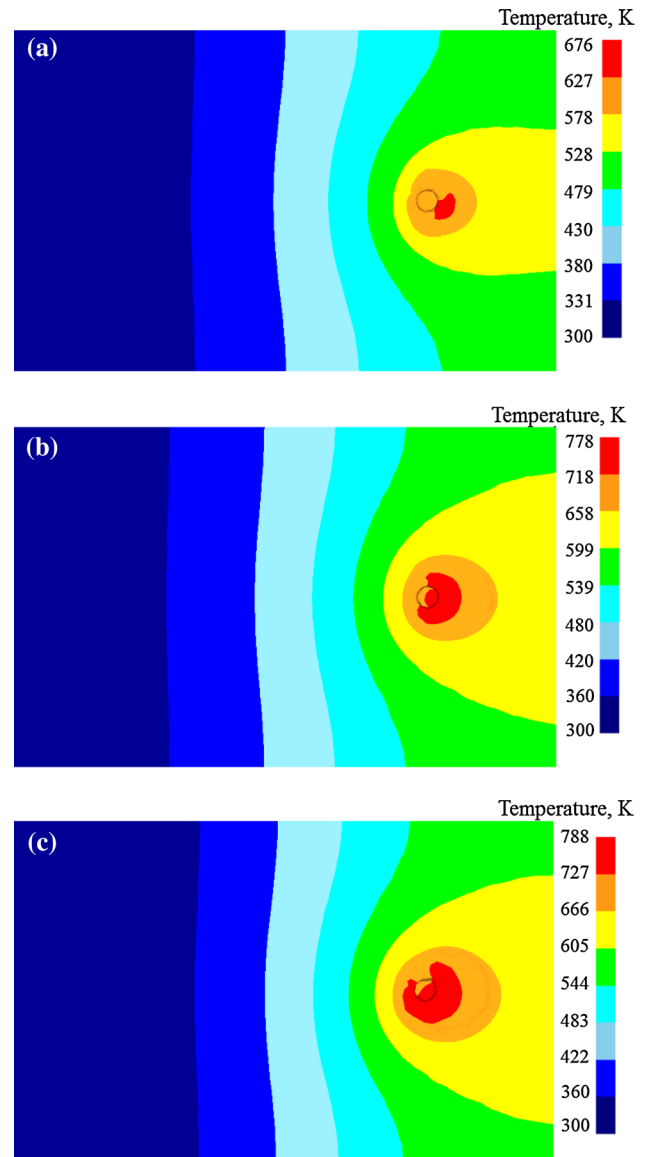
Modeled and experimental conditions	Maximum temperature in SZ	Calculated average MC steps	Predicted average grain size in SZ (μm)	Measured average grain size in SZ (μm) [43]	Error (%)
715 r/min 71.5 mm/min $D = 10$ mm $d = 3$ mm	639 K	124	13.5	12.7	6.2

**Fig. 3** Traced material particles

rotation speed increased from 1000 to 1500 rpm in case 2, the peak temperature reaches 778 K. When the shoulder diameter increases from 10 to 13 mm, the peak temperature reaches 788 K in case 3. Peak temperature histories of the traced material particles in different cases are shown in Fig. 5.

In order to validate the calculated temperature fields, numerical results in case 1 and the experimental observations reported by Buffa [44] are compared. The experimental conditions are the same with case 1. The comparison of the peak temperature profile on the cross section is shown in Fig. 6. As seen in this figure, the calculated temperature profile matches well with both the numerical and experimental results in Ref. [44].

Ten material particles in the middle layer of the work piece with the distance intercept of 0.5 mm are traced in the three cases to study the detail of material flows. Figure 7 shows the movements of particles when the welding tool reaches the particles. In case 1, as shown in Fig. 7a, P1, P2, and P3 at the advancing side are stirred and finally moved back to the advancing side. This flow phenomenon indicates a sufficient material flow, and the defects are not likely to happen at the advancing side by this condition

**Fig. 4** Temperature distributions on welding plates. **a** Case 1, **b** case 2, **c** case 3

[45]. P4 and P5 do not rotate with the tool pin, but experience considerable amounts of deformation. So, P4 and P5 are most likely to belong to the TMAZ. At the retreating

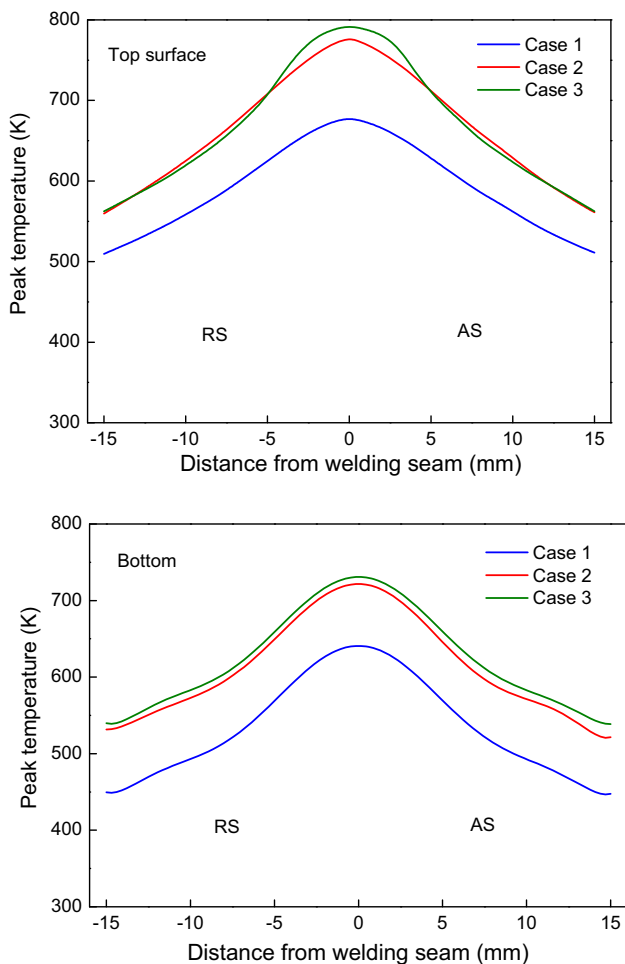


Fig. 5 Temperatures of traced particles along welding seam

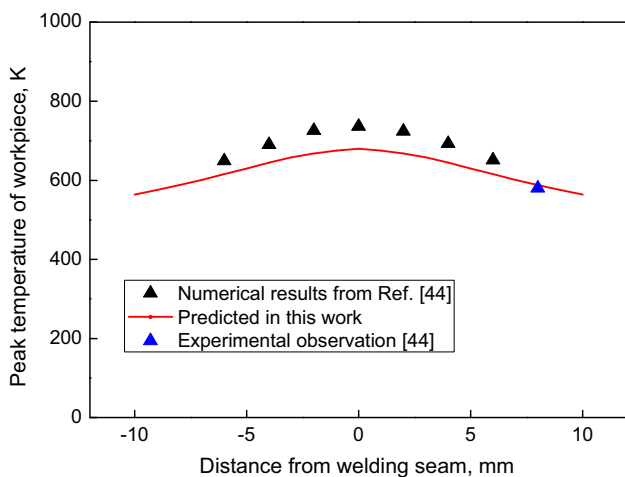


Fig. 6 Validation of peak temperatures in case 1

side, particles have not been stirred to rotate around the pin. P6 moves to nugget zone, although the rest of particles still remain at the retreating side and belong to TMAZ. It

indicates that the welding joint is formed by the materials from the retreating side. These results agree well with the studies of material flows reported by Marzbanrad et al. [46] and Shojaeefard et al. [47].

In case 2 and case 3, as shown in Fig. 7b and c, the ranges of materials particles affected by welding tool are obviously increased with the increase of rotation speed and shoulder diameter. When the rotation speed increases to 1500 r/min in case 2, material particles P1, P3, and P4 are adhered to the stir pin and transverse with the pin for some distance. It indicates that at higher rotation speed, the materials flow more severely and experience larger deformations.

Figure 8 shows the traced material particles on top and bottom surfaces in the three cases after welding. The region of SZ can be determined by the material flows. The width of SZ in each case is summarized in Table 5. Both the increases of rotation speed and the shoulder diameter can lead to the increase of the width of SZ. The grains in HAZ are only affected by heat generation. The movements of the traced material particles are not affected by the stirring effect from the welding tool. This is the criterion for the determination of inner border of HAZ. The outer border of the HAZ is determined by the grain growth process. Between the SZ and the HAZ, the TMAZ exists as a transient region. Certainly, in some cases, TMAZ is ambiguous and hard to determine [2].

TMAZ is quite narrow and can be only distinguished by several particles which are close to the inner border of HAZ. In case 1 shown in Fig. 8a, for example, TMAZ at RS is represented by point P and point Q. The elongated ratio is computed from the distance elongated by the welding tool. The elongated ratios of the two points are 276 and 335 %, respectively. The width of SZ at the bottom surface is narrower than that on top surface. The larger welding tool can obviously increase the width of SZ, as shown in Fig. 8b, c and Table 5.

Simulation of grain growth

Figure 9 shows the simulated grain growth kinetics of the 2D grid systems in different welding zones of the three cases. The values of grain growth exponents in HAZ and TMAZ agree well with 0.41, reported by Anderson et al. [48] and Grest et al. [49] in similar models. The grain growth exponents in SZ are smaller than that in HAZ and TMAZ, and this phenomenon is due to the refinement effects of DRX nuclei. Different thermal cycles and equivalent strain rates lead to different nucleation rates in every MC step, and this causes variations in the growth exponents.

The thermal cycles of the traced material particles together with the annealing times are shown in Fig. 10. At

Fig. 7 Material flows in different cases. **a** Case 1, **b** case 2, **c** case 3

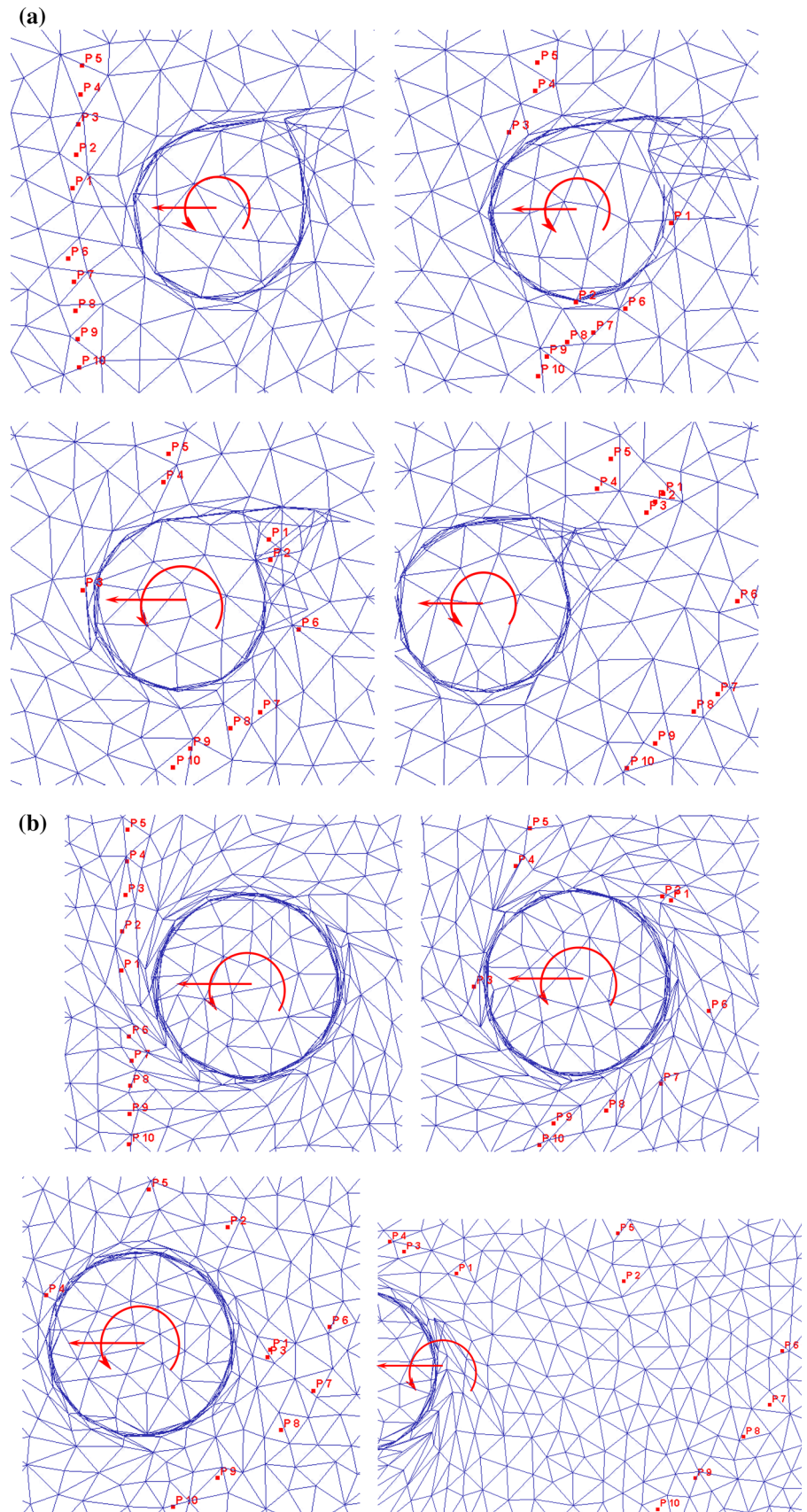
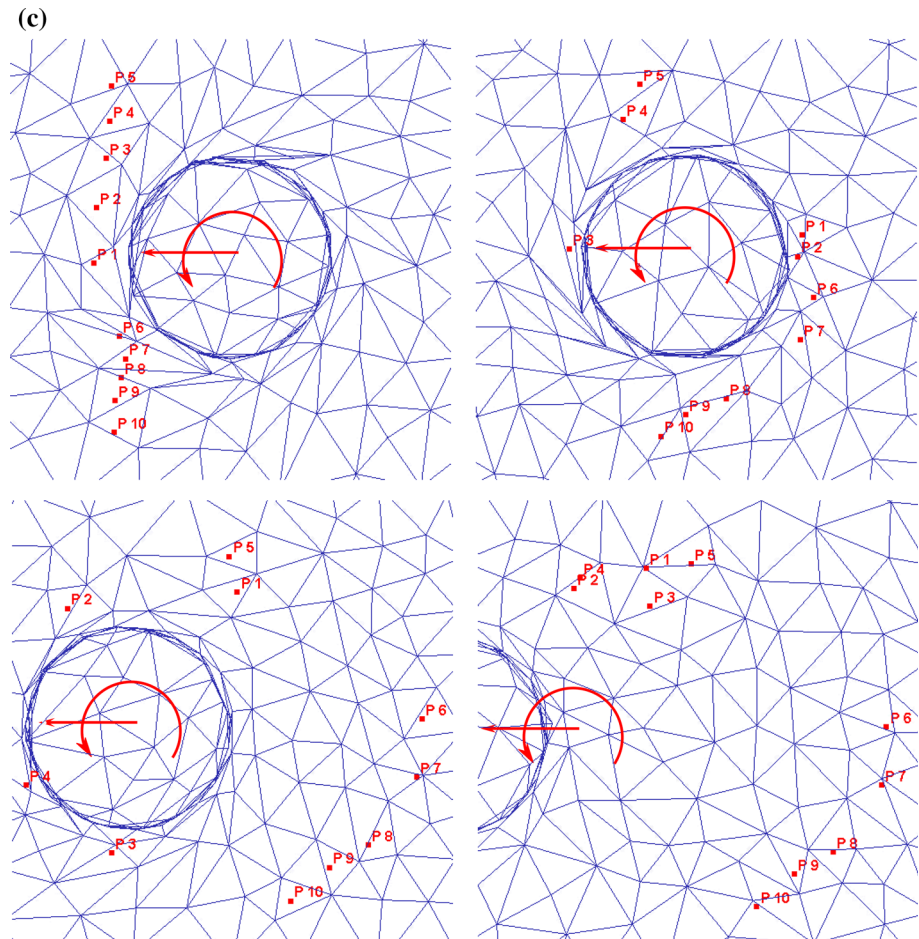


Fig. 7 continued



$t = 0$ s, the temperature starts to raise up and reaches the peak temperature at about $t = 50$ s for case 1. Material particles with higher peak temperatures need more time to cool down to room temperature. Based on the thermal cycles, MC steps of the positions at simulated cross sections can be computed according to Eq. (9).

As described before in the model description part, DRX phenomenon in SZ is affected by the temperature and equivalent strain rate. Figure 11 illustrates the DRX microstructure evolutions in the three cases, 1 mm from welding seam on RS. The nucleation process happen mainly during the high temperature periods, and at the iteration steps in cooling periods with low temperatures, there are nearly no new nuclei to form. In case 1, temperature and equivalent strain rate keep on a low level and the nucleation rate is the smallest, the highest nucleation rate is only 6133 1/mcs at $mcs = 28$. With higher rotation speed and shoulder diameter, the nucleation rates are much higher, reaching 24051 and 19085 1/mcs in case 2 and case 3, respectively. Figure 11 also shows the microstructure in

SZ at the highest nucleation rate points. From the grain-microstructure graphs, the DRX phenomenon can be easily recognized by the small nuclei on the grain boundaries. The density of nucleated cores indicates the nucleation rate in different cases. The nuclei formed from DRX phenomenon also grow during the grain growth simulation, and this is the main effect of grain refinement caused by DRX.

Microstructures of grain growth in 3 cases on top surface are shown as examples in Figs. 12, 13, and 14. Compared to TMAZ, SZ and HAZ are wider and more important in determining the quality of welding joints, thus only SZ and HAZ are investigated in case 2 and case 3 to study the influence of shoulder diameters and rotation speeds.

In SZ, the materials undergo severe plastic flow and broke into fine equiaxed small grains early during the stirring process. The average grain size at the initial time ($MCS = 0$) was $5.4 \mu\text{m}$ in the three cases. Microstructure evolved with the progress of the MC simulation, the

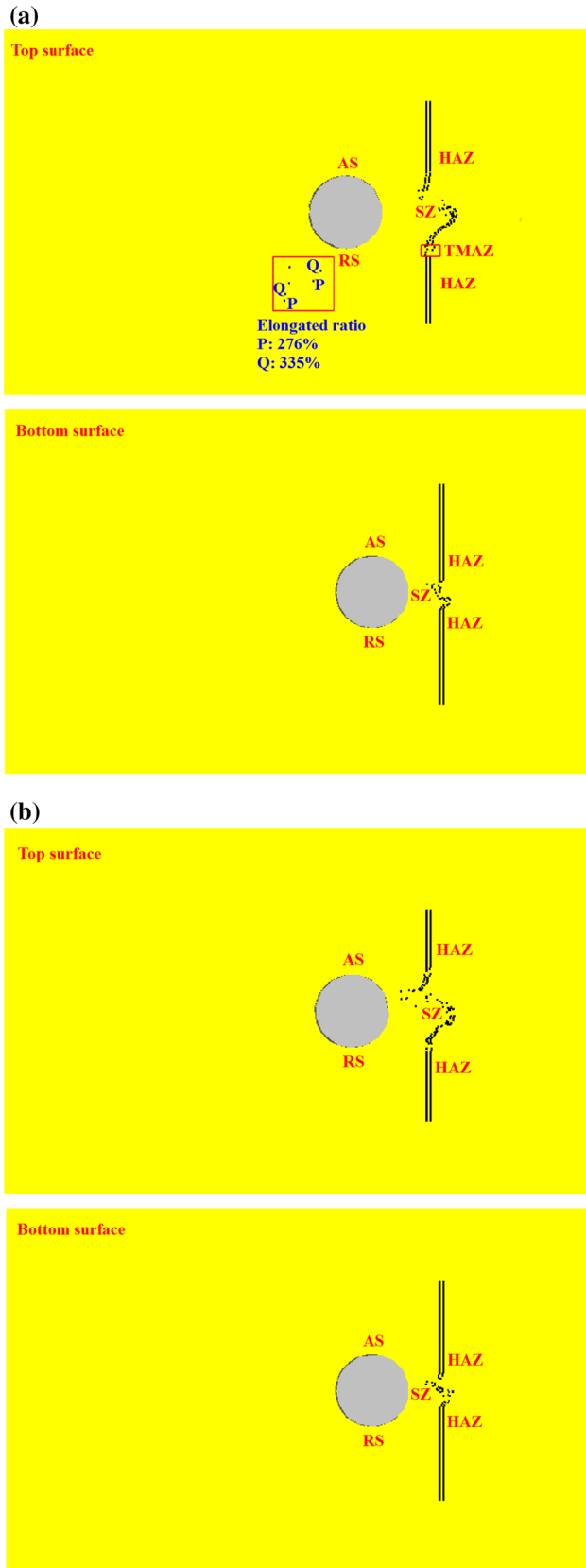


Fig. 8 Traced material particles. a Case 1, b case 2, c case 3

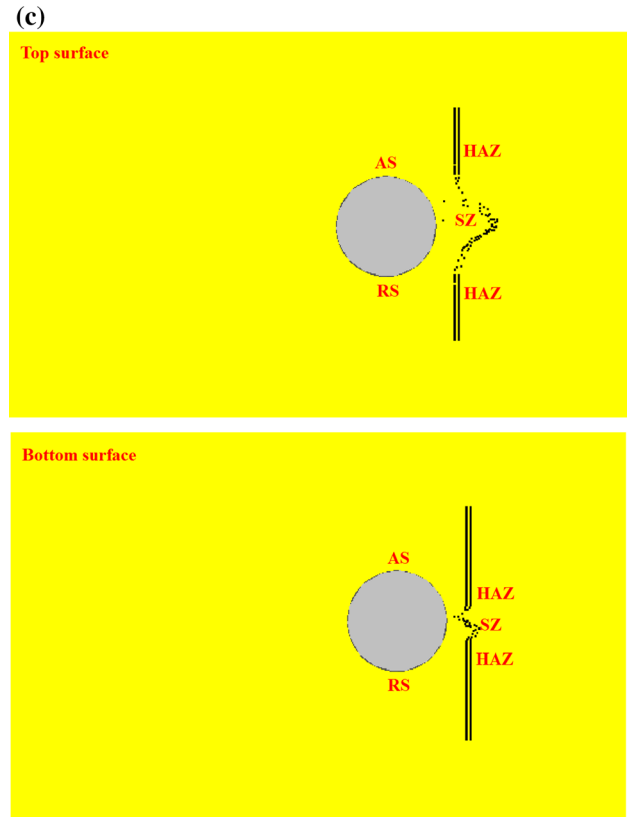


Fig. 8 continued

Table 5 Width of SZ (mm)

	Case 1	Case 2	Case 3
Top surface	8	10	12
Bottom surface	4	4	6

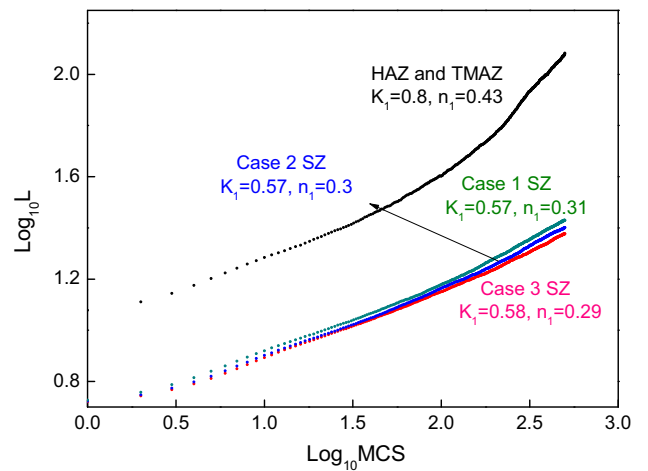


Fig. 9 Growth kinetics of the three cases

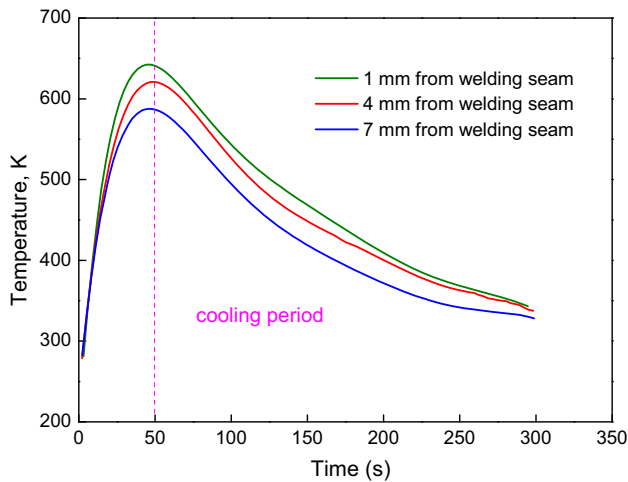


Fig. 10 Temperature histories of traced material particles

average grain size increased visibly as shown in Figs. 12a, 13a, and 14a. Higher rotation speed and larger shoulder led to the increase in temperatures, and also influenced the average grain size in different cases. DRX phenomenon happened during the early periods when the temperature was high, and the DRX phenomenon led to a microstructure consisting of a mixture of large grains and small nuclei, as shown in Fig. 11. But in the cooling periods, the nucleation level decreased quickly. DRX-formed nuclei and normal grains were both simulated to grow according to the same algorithms. The final average grain sizes in SZ of case 1, case 2, and case 3 were 17.6, 18.9, and 20.8 μm , respectively. The average grain sizes can be increased due to the increase of the shoulder diameters and the rotation speeds. This is in accordance with the work reported by Shojaeefard et al. [50]. Similar to the grains in SZ, grains in HAZ were equiaxed grains and their size increased during the post-weld cooling period.

The original grain microstructure of the TMAZ, a narrow zone between the SZ and HAZ, is represented by randomly elongated grains and is shown in Fig. 12b. The evolution of the TMAZ grain microstructure was completed in 90 MC steps, and the average grain size increased from 60.1 to 77.5 μm . The final TMAZ microstructure contained unequiaxed grains, a finding which is consistent with the experimental results of Liu et al. [51].

Figure 15 illustrates the average grain sizes at the simulated cross sections after welding. The FSW-joint is clearly composed of distinct weld zones according to the average grain sizes, as summarized in Table 6. Relationship between the rotation speed and the HAZ width in current work is similar to the optical microscopic investigations reported by Shojaeefard et al. [52]. In the SZ, the average grain sizes are almost uniform in the three cases. The grains on top surface are slightly larger than those on

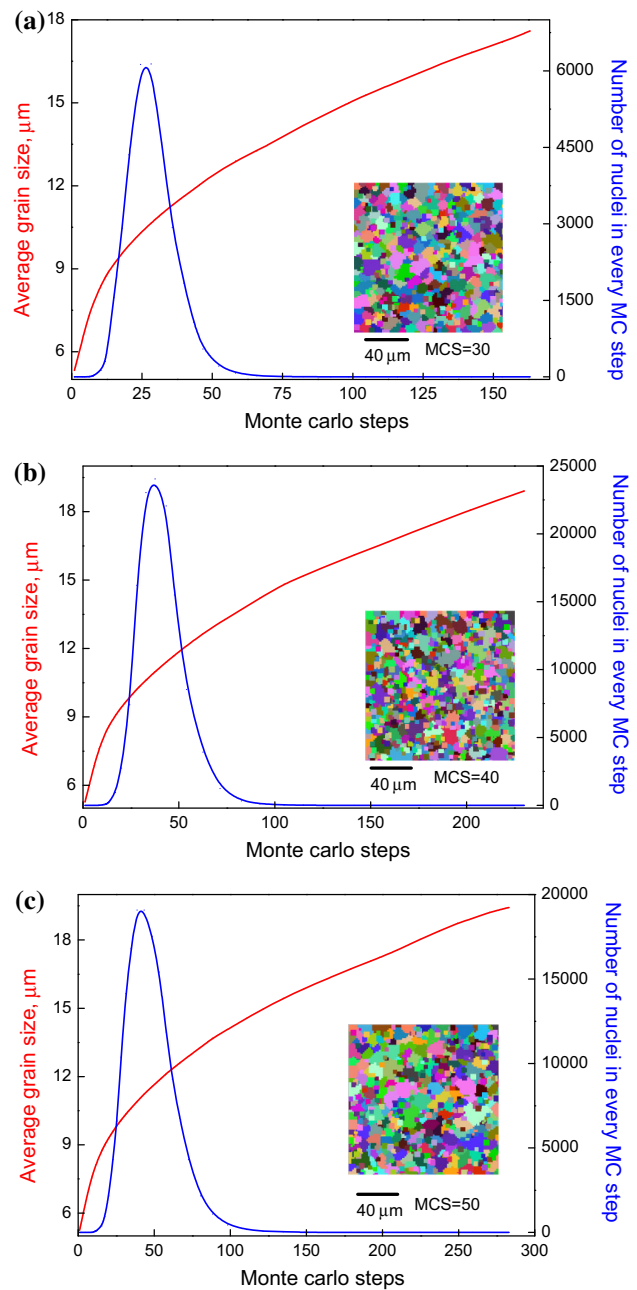
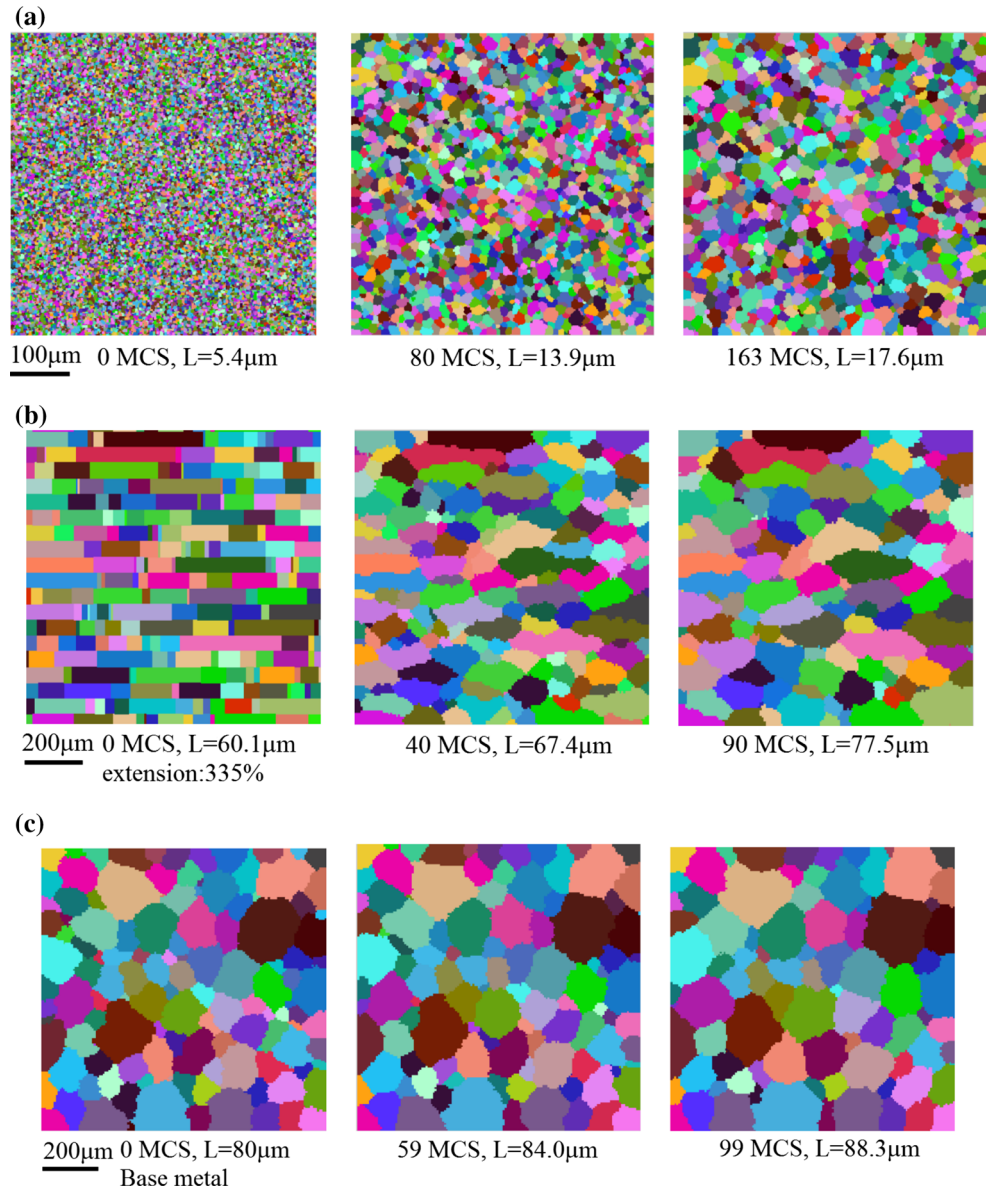


Fig. 11 DRX microstructure evolution in SZ. **a** Case 1, **b** case 2, **c** case 3

the bottom surface; similar results were reported by Chang et al. [41]. Due to the friction between the shoulder and the workpieces, the SZ is wider on the top surface than the bottom surface. The largest grains appear at the inner border of the HAZ. With increasing distance from the welding seam, the grains in the HAZ become smaller and finally transit to grains in base metal at the outer border of the HAZ. Compared to case 1, higher rotation speed and larger shoulder can clearly increase the width of welding zones.

Fig. 12 Microstructure of grain growth in case 1. **a** SZ on top surface, 1 mm from welding seam, RS; **b** TMAZ on top surface, 4.5 mm from welding seam, RS; **c** HAZ on top surface, 5 mm from welding seam, RS



Conclusions

1. Monte Carlo method is employed to simulate the grain growth process in FSW of AA6082-T6.
2. The predicted grain size distributions are symmetrical about the welding seam, and the grain sizes on the top surface of the weld are larger than that those on the bottom surface.
3. Increasing the rotation speed and shoulder diameter can lead to larger grains. Higher rotation speed and larger shoulder can also increase the width of welding zones.
4. It has been demonstrated that the width of the SZ can be estimated by monitoring the motion of traced material particles. The SZ is wider on the top surface of the weld than the bottom surface.
5. The inner border of the HAZ can be determined by material behavior and the outer border can be distinguished by the predicted grain size distribution after welding.

Fig. 13 Microstructure of grain growth in case 2. **a** SZ on top surface, 1 mm from welding seam, RS; **b** HAZ on top surface, 6 mm from welding seam, RS

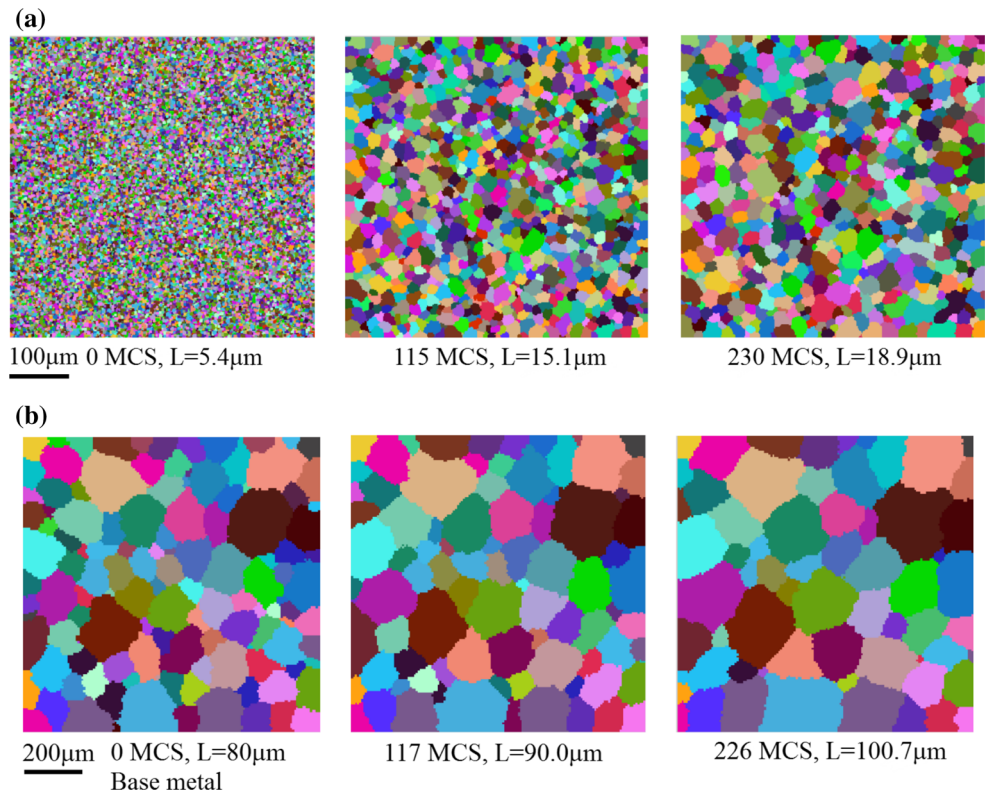
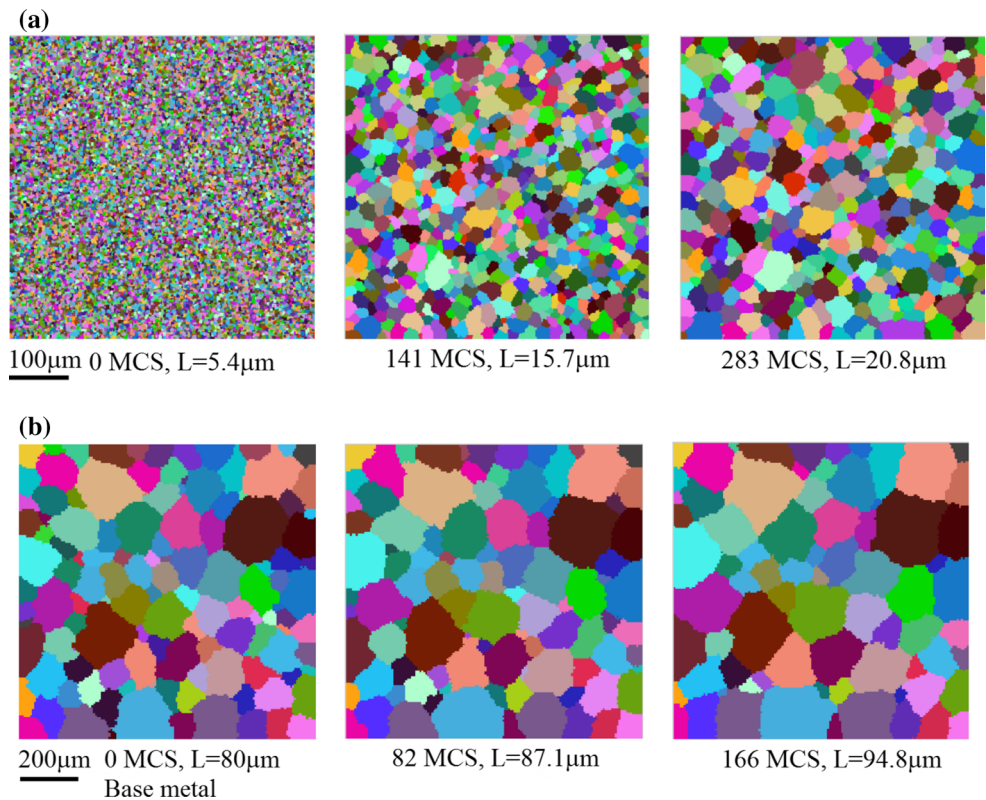


Fig. 14 Microstructure of grain growth in case 3. **a** SZ on top surface, 1 mm from welding seam, RS; **b** HAZ on top surface, 7 mm from welding seam, RS



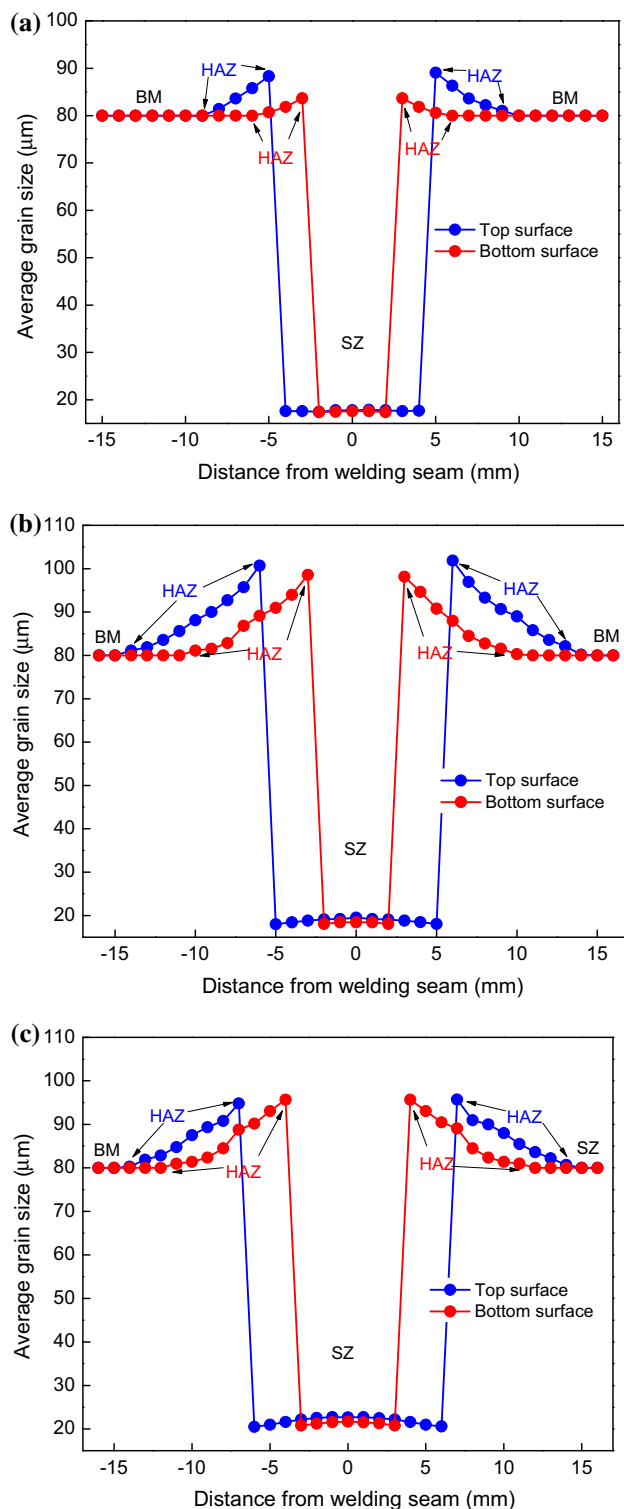


Fig. 15 Distribution of average grain size and welding zones. **a** Case 1; **b** case 2; **c** case 3

Table 6 Width of welding zone (mm)

	Case 1	Case 2	Case 3
Top surface	17	28	28
Bottom surface	10	20	22

Acknowledgement This work was supported by Program for New Century Excellent Talents in University, the Fundamental Research Funds for the Central Universities, the National Natural Science Foundation of China (Nos. 11172057 and 11572074), and the National Key Basic Research Special Foundation of China (2011CB013401).

References

- Mishra RS, Ma ZY (2005) Friction stir welding and processing. *Mater Sci Eng R* 50:1–78
- Nandan R, DebRoy T, Bhadeshia HKDH (2008) Recent advances in friction-stir welding—process, weldment structure and properties. *Prog Mater Sci* 53:980–1023
- Buffa G, Fratini L, Shivpuri R (2007) CDRX modelling in friction stir welding of AA7075-T6 aluminum alloy: analytical approaches. *J Mater Process Technol* 191:356–359
- Grujicic M, Arakere G, Yalavarthy HV, He T, Yen CF, Cheeseman BA (2010) Modeling of AA5083 material-microstructure evolution during butt friction-stir welding. *J Mater Eng Perform* 19:672–684
- Wu LH, Wang D, Xiao BL, Ma ZY (2014) Microstructural evolution of the thermomechanically affected zone in a Ti-6Al-4V friction stir welded joint. *Scripta Mater* 17–20:78–79
- Chen YC, Feng JC, Liu HJ (2009) Precipitate evolution in friction stir welding of 2219-T6 aluminum alloys. *Mater Charact* 60:476–481
- El-Danaf EA, El-Rayes MM (2013) Microstructure and mechanical properties of friction stir welded 6082 AA in as welded and post weld heat treated conditions. *Mater Des* 46:561–572
- Attallah MM, Davis CL, Strangwood M (2007) Microstructure-microhardness relationships in friction stir welded AA5251. *J Mater Sci* 42:7299–7306. doi:10.1007/s10853-007-1585-y
- Sakthivel T, Mukhopadhyay J (2007) Microstructure and mechanical properties of friction stir welded copper. *J Mater Sci* 42:8126–8129. doi:10.1007/s10853-007-1666-y
- Jayaraman M, Balasubramanian V (2013) Effect of process parameters on tensile strength of friction stir welded cast A356 aluminium alloy joints. *Trans Nonferrous Met Soc China* 23:605–615
- Sillapasa K, Surapunt S, Miyashita Y, Mutoh Y, Seo N (2014) Tensile and fatigue behavior of SZ, HAZ and BM in friction stir welded joint of rolled 6N01 aluminum alloy plate. *Int J Fatigue* 63:162–170
- Edwards P, Ramulu M (2015) Fatigue performance of friction stir welded titanium structural joints. *Int J Fatigue* 70:171–177
- Yang Y, Zhou L (2014) Improving corrosion resistance of friction stir welding joint of 7075 aluminum alloy by micro-arc oxidation. *J Mater Sci Technol* 30:1251–1254

14. Rao KP, Ram GDJ, Stucker BE (2008) Improvement in corrosion resistance of friction stir welded aluminum alloys with micro arc oxidation coatings. *Scripta Mater* 58:998–1001
15. Cho HH, Hong ST, Roh JH, Choi HS, Kang SH, Steel RJ, Han HN (2013) Three-dimensional numerical and experimental investigation on friction stir welding processes of ferritic stainless steel. *Acta Mater* 61:2649–2661
16. Pan WX, Li DS, Tartakovsky AM, Ahzi S, Khraisheh M, Khaleel M (2013) A new smoothed particle hydrodynamics non-Newtonian model for friction stir welding: process modeling and simulation of microstructure evolution in a magnesium alloy. *Int J Plasticity* 48:189–204
17. Saluja RS, Narayanan RG, Das S (2012) Cellular automata finite element (CAFE) model to predict the forming of friction stir welded blanks. *Comput Mater Sci* 58:87–100
18. Arora HS, Singh H, Dhindaw BK (2012) Numerical simulation of temperature distribution using finite difference equations and estimation of the grain size during friction stir processing. *Mater Sci Eng A* 543:231–242
19. Simar A, Bréchet Y, Meester B, Denquin A, Gallais C, Pardoën T (2012) Integrated modeling of friction stir welding of 6xxx series Al alloys: process, microstructure and properties. *Progress Mater Sci* 57:95–183
20. Hersent E, Driver JH, Piot D, Desrayaud C (2010) Integrated modeling of precipitation during friction stir welding of 2024-T3 aluminum alloy. *Mater Sci Technol* 26:1345–1352
21. Buffa G, Fratini L, Schneider M, Merklein M (2013) Micro and macro mechanical characterization of friction stir welded Ti-6Al-4V lap joints through experiments and numerical simulation. *J Mater Process Technol* 213:2312–2322
22. Yang Z, Sista S, Elmer JW, DebRoy T (2000) Three Dimensional Monte Carlo simulation of Grain Growth During GTA Welding of Titanium. *Acta Mater* 48:4813–4825
23. Sista S, Yang Z, DebRoy T (2000) Three-dimensional Monte Carlo simulation of grain growth in the heat-affected zone of a 2.25Cr-1Mo steel weld. *Metall Mater Trans B* 31:529–536
24. Ko KJ, Rollett AD, Hwang NM (2010) Abnormal grain growth of Goss grains in Fe-3% Si steel driven by sub-boundary-enhanced solid-state wetting: analysis by Monte Carlo simulation. *Acta Mater* 58:4414–4423
25. Yang W, Chen LQ, Messing GL (1995) Computer simulation of anisotropic grain growth. *Mater Sci Eng A* 195:179–187
26. Taioli S (2014) Computational study of graphene growth on copper by first-principles and kinetic Monte Carlo calculations. *J Mol Model* 20:2260–2272
27. Liu Y, Cheng LF, Zeng QF, Feng ZQ, Zhang J, Peng JH, Xie CW, Guan K (2014) Monte Carlo simulation of polycrystalline microstructures and finite element stress analysis. *Mater Des* 55:740–746
28. Gao JH, Thompson RG (1996) Real time-temperature models for monte carlo simulations of normal grain growth. *Acta Mater* 44:4565–4570
29. Allen JB, Cornwell CF, Devine BD, Welch CR (2013) Simulations of anisotropic grain growth in single phase materials using Q-state Monte Carlo. *Comput Mater Sci* 71:25–32
30. Zhang Z, Wan ZY (2012) Predictions of tool forces in friction stir welding of AZ91 magnesium alloy. *Sci Technol Weld Join* 17:495–500
31. ASM Metals Handbook (1990) Properties and selection: nonferrous alloys and special purpose materials, vol. 2, 10th edn
32. Wei W, Jiang P, Cao F (2013) Constitutive equations for hot deformation of 6082 aluminum alloy. *J Plast Eng* 20:100–106 (in chinese)
33. Asadi P, Akbari M, Karimi-Nemch H (2014) 12—simulation of friction stir welding and processing. In: Givi MKB, Asadi P (eds) *Advances in friction-stir welding and processing*. Woodhead Publishing, Cambridge, pp 499–542
34. Asadi P, Mahdavi-nejad RA, Tutunchilar S (2011) Simulation and experimental investigation of FSP of AZ91 magnesium alloy. *Mater Sci Eng A* 528:6469–6477
35. Zhang Z (2008) Comparison of two contact models in the simulation of friction stir welding process. *J Mater Sci* 43:5867–5877. doi:10.1007/s10853-008-2865-x
36. Huang CM, Joanne CL, Patnaik BSV, Jayaganthan R (2006) Monte Carlo simulation of grain growth in polycrystalline materials. *Appl Surf Sci* 252:3997–4002
37. Driver GW, Johnson KE (2014) Interpretation of fusion and vaporisation entropies for various classes of substances, with a focus on salts. *J Chem Thermodynamics* 70:207–213
38. Yang CC, Rollett AD, Mullins WW (2001) Measuring relative grain boundary energies and mobilities in an aluminum foil from triple junction geometry. *Scripta Mater* 44:2735–2740
39. Kirch DM, Jannot E, Barrales-Mora LA, Molodov DA, Gottstein G (2008) Inclination dependence of grain boundary energy and its impact on the faceting and kinetics of tilt grain boundaries in aluminum. *Acta Mater* 56:4998–5011
40. Ding R, Guo ZX (2001) Coupled quantitative simulation of microstructural evolution and plastic flow during dynamic recrystallization. *Acta Mater* 49:3163–3175
41. Chang CI, Lee CJ, Huang JC (2004) Relationship between grain size and Zener-Holloman parameter during friction stir processing in AZ31Mg alloys. *Scripta Mater* 51:509–514
42. Sato YS, Urata M, Kokawa H (2002) Parameters controlling microstructure and hardness during friction-stir welding of precipitation-hardenable aluminum alloy 6063. *Metall Mater Trans A* 33:625–635
43. Fratini L, Buffa G (2005) CDRX modelling in friction stir welding of aluminium alloys. *Int J Mach Tool Manuf* 45:1188–1194
44. Buffa G, Hua J, Shivpuri R, Fratini L (2006) A continuum based fem model for friction stir welding—model development. *Mater Sci Eng A* 419:389–396
45. Zhang Z, Chen JT (2012) Computational investigations on reliable finite element-based thermomechanical-coupled simulations of friction stir welding. *Int J Adv Manuf Technol* 60:959
46. Marzbanrad J, Akbari M, Asadi P, Safaee S (2014) Characterization of the influence of tool pin profile on microstructural and mechanical properties of friction stir welding. *Metall Mater Trans B* 45:1887–1894
47. Shojaeefard MH, Khalkhali A, Akbari M, Asadi P (2015) Investigation of friction stir welding tool parameters using FEM and neural network. In *Proceedings of the Institution of Mechanical Engineers, Part L: Journal of Materials Design and Applications*, vol 229, pp 209–217
48. Anderson MP, Srolovitz DJ, Grest GS, Sahni PS (1984) Computer simulation of grain growth—I. Kinetics. *Acta Metall* 32:783–791
49. Grest GS, Anderson MP, Srolovitz DJ (1988) Domain-growth kinetics for the Q-state Potts model in two and three dimensions. *Phys Rev B* 38:4752–4760
50. Shojaeefard MH, Akbari M, Khalkhali A, Asadi P, Parivar AH (2014) Optimization of microstructural and mechanical properties of friction stir welding using the cellular automaton and Taguchi method. *Mater Des* 64:660–666
51. Liu L, Nakayama H, Fukumoto S, Yamamoto A, Tsubakino H (2004) Microstructural evolution in friction stir welded 1050 aluminum and 6061 aluminum alloy. *Mater Trans* 45:2665–2668
52. Shojaeefard MH, Akbari M, Asadi P (2014) Multi objective optimization of friction stir welding parameters using FEM and neural network. *Int J Precis Eng Manuf* 15:2351–2356